INL/JOU-20-60662-Revision-0

Automatic Information Extraction from Neutron Radiography Imaging to Estimate Axial Fuel Expansion in EBR-II

December 2021

Andrei V Gribok, Douglas L Porter, Kyle Mitchell Paaren, Micah D Gale,
Nancy J Lybeck, Scott C Middlemas

INL/JOU-20-60662-Revision-0

Automatic Information Extraction from Neutron Radiography Imaging to Estimate Axial Fuel Expansion in EBR-II

Andrei V Gribok, Douglas L Porter, Kyle Mitchell Paaren, Micah D Gale, Nancy J Lybeck, Scott C Middlemas

December 2021

Idaho National Laboratory
Idaho Falls, Idaho 83415

http://www.inl.gov

Prepared for the
U.S. Department of Energy
Under DOE Idaho Operations Office
Contract DE-AC07-05ID14517

Automatic Information Extraction from Neutron Radiography Imaging to Estimate Axial Fuel Expansion in EBR-II

Andrei V. Gribok, Douglas L. Porter, Kyle M. Paaren, Micah D. Gale, Scott C. Middlemas, Nancy J. Lybeck

Idaho National Laboratory, Idaho Falls, Idaho, 83415

Abstract

Approximately 130,000 metal fuel pins were irradiated in the Experimental Breeder Reactor II (EBR-II) during its 30 years of operation to develop and characterize existing and prospective fuels. For many of the metal fuel irradiation experiments, neutron radiography imaging was performed to characterize fuel behavior, like fuel swelling. However, due to the lack of technology or resources, many of the images have not been processed or were processed manually through visual examination. This paper represents first-attempt efforts to develop an image processing algorithm capable of automatically extracting information regarding the degree of fuel swelling from neutron radiography imaging. This algorithm was applied to 120 images of three different metallic fuel pin compositions—U-10Zr, U-8Pu-10Zr, and U-19Pu-10Zr. The algorithm performs operations of image intensity adjustment, image binarization, region finding, and labeling to extract information about fuel swelling. The average growth for U-10Zr was found to be 8.49% with 95% Confidence Interval (CI) [8.33 –8.66%], for U-8Pu-10Zr — 7.50% with 95% CI [7.23 – 7.78%],and for U-19Pu-10Zr — 3.15%, with 95% CI [2.40 – 3.91%]. The results obtained by applying this automatic image processing algorithm are consistent with previously reported studies of the same types of fuels. The automatic image processing algorithm will be expanded to include thousands of available neutron radiography images and different types of fuels to investigate empirical dependencies of fuel swelling, which can be subsequently applied to advanced fuel modeling. Results from this study will later be compared to BISON simulations to further benchmark modeling efforts and develop assessment cases.

1. Introduction

In its 30 year history, the Experimental Breeder Reactor II (EBR-II) — an irradiation facility for metal fuel development — underwent a number of transformations starting as a demonstration test bed for a closed loop fuel cycle, evolving into the Integral Fast Reactor (IFR) program [1]. Fuel technology is a key aspect of sodium-cooled fast reactor (SFR) systems, affecting reactor safety, reactor operations, fuel reprocessing technology, and overall system economics [2]. Two major types of fuel were extensively studied and qualified as driver fuels for SFRs in the United States (U.S.) and around the world, mixed oxide fuel (MOX) and metallic fuel.

One advantage of metallic fuels is their higher thermal conductivity with a highly conductive gap (liquid metal) that enables the fuel to operate at lower temperatures with reduced stored energy. In addition, metallic fuels have a more favorable neutron economy, higher fuel densities, and easier fabrication and reprocessing processes [1]. The disadvantage of metallic fuels was their relatively low burnup limit in comparison with MOX fuels; however, U-19Pu-10Zr can achieve 110 gigawatt-days/metric ton of heavy metal (GWD/MTHM) if operated on a three burn cycle, while MOX fuel will max out at 65 GWD/MTHM. In this paper, we consider U-10Zr, U-8Pu-10Zr, and U-19Pu-10Zr fuel compositions within the EBR-II fuel pins.

Regardless of the type of fuel, the timeline for qualification of advanced nuclear fuel design is inordinately prolonged by the costs and inefficiencies in generating, analyzing, and modeling nuclear experimental data. For example, a single nuclear fuel or materials experiment may contain relatively few experimental specimens, yet cost as much as $5 to $10 M each, require more than five years per cycle, and require four to five experiment cycles to obtain satisfactory qualification data (i.e., 20–25 years in total) [3]. Crawford et al. [1] have outlined the steps for qualification, indicating that it takes 20–25 years for complete development and licensing for metallic fuels. The research effort presented in this paper is directed towards shortening the development time and accelerating the licensing process for fuel, as this research's success applied to a given fuel performance characteristic is transferable to other key fuel characteristics and to other fuel types as knowledge and proficiency increase.

The EBR-II dataset is comprehensive, as it combines a great range of experiments with different fuel alloys, cladding types, and geometric characteristics leading to the qualification of sodium-bonded U-10Zr fuel in EBR-II, and provides data that could be used for other metal fuel designs for advanced SFRs. Some publications show data analysis from a few of the SFR fuel experiments [4–10], but much of the data has not been reported, analyzed, or even segregated into a usable form.

The many terabytes of experimental data that have been generated cannot make a technologically meaningful impact on a short time scale without the means for their rapid conversion to knowledge; hence, much of the data are not effectively fed back into the research and development (R&D) cycle. Furthermore, our stored historical fast reactor data, analysis tools, and modeling and simulation suite Multiphysics Object Oriented Simulation Environment (MOOSE) and its derivatives—Mesoscale Fuel Performance Code and Engineering Scale Fuel Performance Code (MARMOT-BISON) collectively known as (MBM)—are currently decoupled from each other, making it extremely cumbersome to develop a fundamental understanding of the relationships between experimental parameters and response data. Although powerful "big data" tools are commercially available, many of these "off-the-shelf" solutions are chiefly designed for business analytics. The scale, complexity, and heterogeneity of irradiation experimental data make them untenable for impactful scientific analysis. The conversion of this archived data is paramount to the development of next generation nuclear reactors in the U.S. and abroad.

The goal of this paper is to make initial steps towards automating the processing of archived datasets. In this case, using targeted data metallic fast reactor fuel analysis and feeding it into a database specifically designed to provide information ports envisioned to be necessary for modeling of fuel performance or fuel qualification is the purpose of our research. The case in point is the SFR metal fuel database, which contains many neutron radiographs of as-irradiated test fuel pins. A primary use for that data is the measurement of axial fuel growth, which needs to be measured and linked to starting fuel geometry and composition, as well as the operating conditions of the pin. The radiography analyzed for specific interests then provide raw data from which a model for axial fuel growth can be further developed in BISON or a fuel condition predicted to support a case for fuel qualification, or both.

The major thrust of the current effort is demonstrating how automated image processing algorithms can be developed to extract information about axial fuel growth from neutron radiographs. This information can be fed to models allowing for predictive capacity beyond existing functional datasets, such as burnup in relation to porosity and fission gas release. A predictive capability presents the best prospects to enhance credibility of parametric sensitivity analyses of variables such as smeared density, burnup, etc. Such a predictive capability would in turn help to select the more important experiments that should be performed while ruling out others, and help to identify meaningful durations of experiments, thereby shortening development time. Continuing success with a predictive capability would increase the acceptance of extrapolated behaviors for inclusion in documentation provided to review bodies.

2. Data and Materials

2.1 Neutron Radiography

To demonstrate potential for automated image processing, 20 EBR-II neutron radiography images were used. Each image contained six fuel pins with different fuel compositions. Detailed technical specification of the pins is presented in Table 1.

Table 1. Summary of analyzed fuel pins.

Experiment ID	Pin ID	Fuel Composition	Cladding Type	Fuel Slug Length [cm]	Average Burnup [at%]	Peak Burnup* [at%]
X425A	T409	U-10Zr	HT9	34.34	8.22	9.21
X425A	T444	U-8Pu-10Zr	HT9	34.42	14.89	16.56
X425A	T473	U-19Pu-10Zr	HT9	34.44	15.44	17.20
X425A	T445	U-8Pu-10Zr	HT9	34.42	14.90	16.57
X425A	T411	U-10Zr	HT9	34.32	8.16	9.15
X425A	T413	U-10Zr	HT9	34.32	15.19	16.88
X425A	T414	U-10Zr	HT9	34.34	15.26	16.93
X425A	T446	U-8Pu-10Zr	HT9	34.44	14.98	16.65
X425A	T486	U-19Pu-10Zr	HT9	34.37	6.60	7.20
X425A	T416	U-10Zr	HT9	34.34	8.56	9.29
X425A	T492	U-8Pu-10Zr	HT9	34.32	6.50	7.09
X425A	T478	U-10Zr	HT9	34.32	6.46	7.04
X425A	T475	U-19Pu-10Zr	HT9	34.19	9.05	9.83
X425A	T477	U-10Zr	HT9	34.32	15.63	17.37
X425A	T435	U-10Zr	HT9	34.34	8.98	9.75
X425A	T479	U-10Zr	HT9	34.32	15.74	17.49
X425A	T456	U-8Pu-10Zr	HT9	34.34	8.92	9.68
X425A	T422	U-10Zr	HT9	34.32	15.75	17.51
X425A	T498	U-8Pu-10Zr	HT9	34.34	6.58	7.17
X425A	T499	U-8Pu-10Zr	HT9	34.44	6.57	7.17
X425A	T425	U-10Zr	HT9	34.32	15.39	17.10
X425A	T467	U-19Pu-10Zr	HT9	34.44	8.76	9.51
X425A	T493	U-8Pu-10Zr	HT9	34.44	6.54	7.13
X425A	T426	U-10Zr	HT9	34.34	15.45	17.16
X425B	E767	U-10Zr	HT9	34.29	5.05	5.49
X425B	E416	U-10Zr	HT9	34.29	5.10	5.55
X425B	E790	U-10Zr	HT9	34.29	4.98	5.40
X425B	E834	U-10Zr	HT9	34.29	4.70	5.28
X425B	E456	U-10Zr	HT9	34.29	4.93	5.36
X425B	E770	U-10Zr	HT9	34.29	4.73	5.31
X425B	F370	U-10Zr	HT9	34.29	5.02	5.45
X425B	F446	U-10Zr	HT9	34.29	5.14	5.59
X425B	E779	U-10Zr	HT9	34.29	5.06	5.49
X425B	F393	U-10Zr	HT9	34.29	5.08	5.52
X425B	F404	U-10Zr	HT9	34.29	5.11	5.55

Experiment ID	Pin ID	Fuel Composition	Cladding Type	Fuel Slug Length [cm]	Average Burnup [at%]	Peak Burnup* [at%]
X425B	F366	U-10Zr	HT9	34.29	5.16	5.61
X425B	F418	U-10Zr	HT9	34.29	4.81	5.23
X425B	E816	U-10Zr	HT9	34.29	4.83	5.26
X425B	E814	U-10Zr	HT9	34.29	4.88	5.32
X425B	E843	U-10Zr	HT9	34.29	4.91	5.35
X425B	F355	U-10Zr	HT9	34.29	4.68	5.25
X425B	F427	U-10Zr	HT9	34.29	4.97	5.41
X425B	T420	U-10Zr	HT9	34.32	12.60	14.04
X425B	T493	U-8Pu-10Zr	HT9	34.44	6.54	7.13
X425B	T450	U-8Pu-10Zr	HT9	34.37	12.75	14.22
X425B	T497	U-8Pu-10Zr	HT9	34.37	6.65	7.25
X425B	T500	U-8Pu-10Zr	HT9	34.42	6.65	7.25
X425B	T431	U-10Zr	HT9	34.34	12.77	14.24
X425B	T421	U-10Zr	HT9	34.34	12.64	14.08
X425B	T426	U-10Zr	HT9	34.34	12.74	14.19
X425B	T496	U-8Pu-10Zr	HT9	34.34	6.58	7.18
X425B	T498	U-8Pu-10Zr	HT9	34.34	6.58	7.17
X425B	T499	U-8Pu-10Zr	HT9	34.44	6.57	7.17
X425B	T425	U-10Zr	HT9	34.32	12.68	14.14
X425B	T440	U-8Pu-10Zr	HT9	34.29	11.98	13.38
X425B	T401	U-10Zr	HT9	34.32	12.24	13.63
X425B	T441	U-8Pu-10Zr	HT9	34.34	12.10	13.51
X425B	T442	U-8Pu-10Zr	HT9	34.42	12.11	13.52
X425B	T402	U-10Zr	HT9	34.34	12.28	13.69
X425B	T404	U-10Zr	HT9	34.34	12.37	13.78
X425B	T444	U-8Pu-10Zr	HT9	34.42	12.22	13.63
X425B	T473	U-19Pu-10Zr	HT9	34.44	12.67	14.17
X425B	T445	U-8Pu-10Zr	HT9	34.42	12.23	13.65
X425B	T405	U-10Zr	HT9	34.34	12.39	13.81
X425B	T413	U-10Zr	HT9	34.32	12.49	13.91
X425B	T414	U-10Zr	HT9	34.34	12.53	13.95
X425B	T446	U-8Pu-10Zr	HT9	34.44	12.31	13.73
X425B	T486	U-19Pu-10Zr	HT9	34.37	6.60	7.20
X425B	T408	U-10Zr	HT9	34.34	12.52	13.95
X425B	T492	U-8Pu-10Zr	HT9	34.32	6.50	7.09
X425B	T478	U-10Zr	HT9	34.32	6.46	7.04
X425B	T447	U-8Pu-10Zr	HT9	34.37	12.58	14.04
X425B	T477	U-10Zr	HT9	34.32	12.92	14.41
X425B	T466	U-10Zr	HT9	34.32	12.86	14.34
X425B	T436	U-10Zr	HT9	34.32	6.73	7.34
X425B	T479	U-10Zr	HT9	34.32	13.02	14.52
X425B	T455	U-8Pu-10Zr	HT9	34.37	12.89	14.39

Experiment ID	Pin ID	Fuel Composition	Cladding Type	Fuel Slug Length [cm]	Average Burnup [at%]	Peak Burnup* [at%]
X425B	T438	U-10Zr	HT9	34.34	13.01	14.51
X425B	T491	U-19Pu-10Zr	HT9	34.42	6.74	7.35
X425B	T451	U-8Pu-10Zr	HT9	34.34	12.78	14.26
X425B	T494	U-8Pu-10Zr	HT9	34.44	6.72	7.33
X425B	T424	U-10Zr	HT9	34.32	6.67	7.27
X425B	T470	U-19Pu-10Zr	HT9	34.29	13.11	14.66
X425B	T453	U-8Pu-10Zr	HT9	34.37	12.80	14.29
X430	T652	U-19Pu-10Zr	HT9	34.44	9.30	10.08
X430	T686	U-10Zr	HT9	34.39	9.54	10.34
X430	T653	U-19Pu-10Zr	HT9	34.42	9.15	9.91
X430	T687	U-10Zr	HT9	34.42	4.05	4.43
X430	T688	U-10Zr	HT9	34.42	9.68	10.48
X430	T689	U-10Zr	HT9	34.42	9.08	10.16
X430	T657	U-19Pu-10Zr	HT9	34.44	7.66	8.33
X430	T662	U-10Zr	HT9	34.42	4.02	4.39
X430	T692	U-10Zr	HT9	34.42	9.04	10.12
X430	T693	U-10Zr	HT9	34.44	3.95	4.33
X430	T694	U-10Zr	HT9	34.21	9.58	10.37
X430	T681	U-10Zr	HT9	34.42	4.08	4.45
X430	T690	U-10Zr	HT9	34.44	4.21	4.59
X430	T654	U-19Pu-10Zr	HT9	34.42	9.32	10.09
X430	T710	U-10Zr	HT9	34.39	8.99	10.07
X430	T711	U-10Zr	HT9	34.39	4.13	4.51
X430	T709	U-10Zr	HT9	34.42	9.65	10.45
X430	T655	U-19Pu-10Zr	HT9	34.29	9.46	10.25
X430	T696	U-10Zr	HT9	34.42	4.05	4.43
X430	T658	U-19Pu-10Zr	HT9	34.44	9.20	9.97
X430	T697	U-10Zr	HT9	34.34	8.92	9.98
X430	T698	U-10Zr	HT9	34.39	9.65	10.44
X430	T679	U-10Zr	HT9	34.42	4.14	4.52
X430	T659	U-19Pu-10Zr	HT9	34.42	9.37	10.15
X430	T700	U-10Zr	HT9	34.26	4.09	4.47
X430	T663	U-10Zr	HT9	34.32	9.40	10.18
X430	T702	U-10Zr	HT9	34.39	8.89	9.96
X430	T666	U-10Zr	HT9	34.37	4.22	4.60
X430	T660	U-19Pu-10Zr	HT9	34.42	9.52	10.31
X430	T685	U-10Zr	HT9	34.42	4.17	4.56
X430	T704	U-10Zr	HT9	34.42	9.54	10.33
X430	T705	U-10Zr	HT9	34.42	9.05	10.13
X430	T651	U-10Zr	HT9	34.44	9.00	10.07
X430	T706	U-10Zr	HT9	34.44	4.32	4.71
X430	T707	U-10Zr	HT9	34.44	9.53	10.32

Experiment ID	Pin ID	Fuel Composition	Cladding Type	Fuel Slug Length [cm]	Average Burnup [at%]	Peak Burnup* [at%]
X430	T708	U-10Zr	HT9	34.39	4.27	4.66
* Burnup segments were calculated axially in lengths of cm.						

The parameter of interest in this study is the extent of axial growth of fuel pins, which needs to be estimated for use in manufactured measurements for modeling predictions. The axial growth of metallic fuel is caused primarily by increasing porosity due to trapped internal fission gas bubbles as the U-xPu-10Zr fuel burns. The axial growth of the fuel pins can be measured either by visually examining the neutron radiography images or by using axial gamma scans.

Several different radioisotopes are measured for the gamma scan measurements, with Rhodium isotopes being particularly useful in measuring fuel length. Rhodium-106 is a fission product that tends to stay with the fuel material as it expands, thus making it a good indicator of where fuel is within the pin on a gamma scan spectrum [3]. However, the gamma scanning equipment had a positioning accuracy of 1 cm, which is within the measurable difference for different types of fuels, thus making this technique highly uncertain for fuels with similar compositions. On the other hand, neutron radiography is performed with a high precision scale graduated to 0.02 in. or 0.051 cm placed next to the fuel pin, and hence, the fuel growth can be more accurately determined by visual examination. The disadvantage of the neutron radiograph is the ambiguity of the exact location of the fuel pin's top as it is distorted during the irradiation process, creating areas with low fuel densities colloquially referred as "fluff." The presence of "fluff" at the top of the fuel pins requires visual analysis of the radiograph image by an expert and makes the analysis non-conducive to automation. This paper aims to address this problem using image processing tools to significantly speed up the process of image analysis and remove the human factor bias.

The irradiated metallic fuel pins discussed in this paper were radiographed using dysprosium foil detectors most sensitive to thermal neutrons. The activated foils were then used to transfer images to film. The thermal neutrons provide images with better contrast at the expense of more shallow penetration of the fuel. For this paper, the higher contrast images are indispensable and were favored over epithermal neutron imaging. Detailed description of neutral radiography imaging can be found in Reference [12]. Images on film were subsequently digitized using a scanner to obtain images in a JPEG format. These JPEG images were used as original images for the image processing algorithms presented in the paper.

3. Image Processing

3.1 Image Conversion

Recent advances in image processing and computer vision demonstrated in such diverse fields as biomedical research [13], material science [14], security, and traffic control [15] offer an opportunity to automate analysis of thousands of images—thus reducing time and efforts to validate different types of fuels. Image analysis has been used in nuclear engineering to solve diverse problems in fuel development, manufacturing, and analysis [17 – 22]. However, few efforts were undertaken to develop an automatic information extraction pipeline specifically for fuel qualification. The research presented in this paper attempts to fill that gap.

The original JPEG images of neutron radiography were acquired with 150 dpi resolution using 35 mm focal length, and on average have the size of 4,300 by 10,000 pixels with color depth of 24 bits. The JPEG image format uses a compression algorithm to store the image; however, it is decompressed while being loaded into RAM and takes the same amount of RAM as lossless formats such as TIFF. The original JPEG images use RGB color coding, which requires three bytes to represent each pixel. Since the neutron radiographs have no meaningful color information, the RGB images prior to processing have been converted into grayscale images. Each channel in RGB image has 256 shades, the RGB image is converted into grayscale by taking the weighted sum of the R, G, and B values, specifically. For this paper, the conversion formula is:

$$\mathrm{Gray} = 0.2989 \times \mathrm{R} + 0.5870 \times \mathrm{G} + 0.1140 \times \mathrm{B} \quad (1)$$

The triplet of weights (0.2989, 0.5870, 0.1140) used in the conversion formula, comes from BT.601-7 [16] recommendations developed by the International Telecommunication Union. Since all three channels in the grayscale image are set to the same level, only one byte is necessary to store each pixel—thus reducing RAM requirements by a factor of three.

The general pipeline of image processing used in this paper is shown in Figure 1. After reading an image into RAM, the original image is converted into a grayscale image. The next step is to adjust the image intensity or contrast so that the signal-to-noise ratio can be improved. After this contrast adjustment, image binarization is performed to remove gray areas and perform image segmentation. Since binarization is a nonlinear operation, it performs all or nothing filtering, setting gray areas either as white pixels or black pixels. Using a binary image from a previous step, a connectivity algorithm is applied to detect connected areas of white pixels. Since most white pixels will represent the fuel, the connectivity operation effectively segments the image into the foreground and background. Further, each foreground region of the image is labeled to attribute it to a pin.

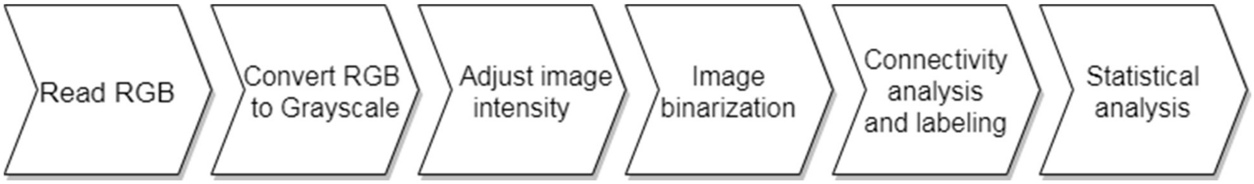

Figure 1. Flow chart of image processing steps.

Smaller foreground regions are eliminated by setting them to the background, thus removing objects that are not part of the fuel pins. Having labeled the image regions, the algorithm groups the labeled objects by pin. The length of the fuel pins is then calculated, and statistical analysis is performed to segregate pins with different fuel compositions and to determine corresponding axial fuel growth. These image processing steps are further described in the following sections in more detail. Codes designed to characterize fuel growth were developed using MATLAB's Image Processing Toolbox.

3.2 Adjusting Image Intensity

A neutron radiography image of pins T446, T486, T408, T492, T478, and T447 from experiment X425B is shown in Figure 2. The color bar is placed next to the image to represent grayscale color mapping to pixel values. Since grayscale image pixel values range from 0-black to 255-white, each value in that range is mapped into a shade of gray, with an assumption that black and white colors are extreme representation of gray. As can be seen from the image, the very top of the fuel pins is distorted due to axial growth, with accurate and automatic determination of the axial fuel growth bearing a challenge due to the "fluff" at the top of the fuel pins. To the left of the fuel pins, a high precision ruler is placed to estimate changes in fuel configuration.

The image contrast or intensity is defined as the difference between the brightest and darkest pixels [23]. To increase image contrast, the enhancement algorithms usually saturate a given percentage of pixels from the bottom and top of the grayscale—thus "stretching" the image pixel values, as shown in Figure 3.

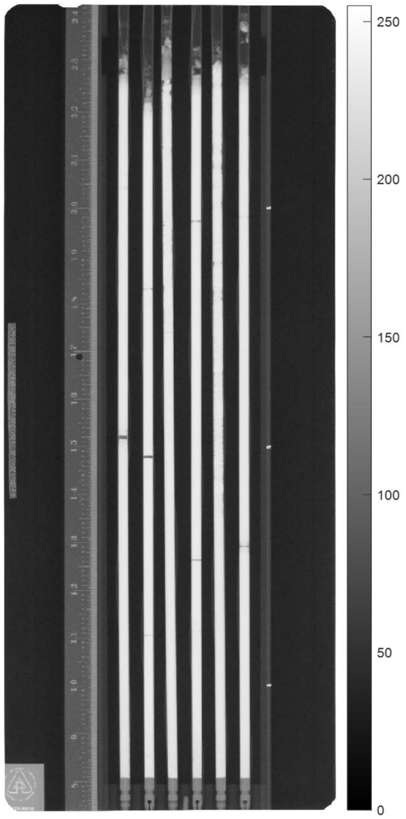

Fig. 2 Original grayscale radiography image of X425B, pins T446, T486, T408, T492, T478, and T447 (left to right). The six pins (left to right) have the following fuel compositions: U-8Pu-10Zr, U-19Pu-10Zr, U-10Zr, U-8Pu-10Zr, U-10Zr, and U-8Pu-10Zr.

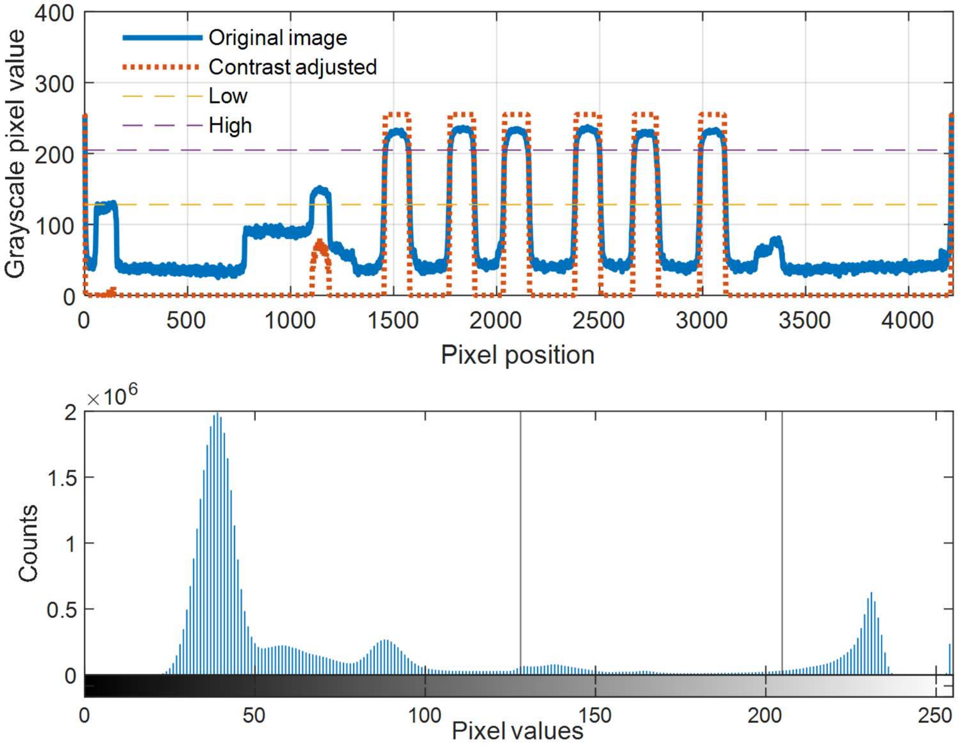

Figure 3. Cross section of a grayscale neutron radiography image of X425B before and after contrast enhancement (top panel) and image histogram (bottom panel). The low and high intensity mapping thresholds are also shown.

For this paper, the saturation limits were set at 50% for low intensity pixels and 20% for high intensity pixels, which means that pixels with intensity values less than 128 were mapped to zero, while pixels with intensity values higher than 205 were mapped to 255. The intensity values between 128 and 205 are linearly mapped into the 0 – 255 range.

The selection of threshold intensity values was performed based on analysis of the image histograms as shown in the bottom panel of Fig. 3. As can be seen from the histogram, the high intensity threshold of 205 saturates the brightest pixels corresponding to the rightmost mode of the histogram. The low intensity threshold of 128 sets the majority of the dark pixels to zero. Since all images in this study have very similar structure and consequently histograms, the intensity enhancement thresholds can be set to the same value for all images.

The purpose of performing contrast adjustment is to improve the signal-to-noise ratio (SNR). In neutron radiograph imaging, the signal refers to the pixels representing the fuel pins while the noise is the black background. As can be seen from Figure 3, the pin pixels have values very close to 255, which correspond to pure white. On the other hand, the background pixels are set around a grayscale value of 50 or lower, which is dark gray. The difference between the lowest pixel values and the highest ones for the original image is about 200, while for the contrast-adjusted image it is 255.

An additional benefit of performing contrast adjustment is the removal of gray areas, such as a ruler placed next to the pins. Original and contrast-adjusted images are shown side-to-side in Figure 4. As can be seen from the figure, the contrast-adjusted image has fewer gray areas with more visible cracks in the pins, as well as some low-density fuel “fluff” and fission products (Cs-133, Cs-137) removed from the top of the pins. While the contrast-adjusted image has a better SNR, it still retains some gray areas that are either not a part of the fuel pins or represent the fuel disintegration “fluff” areas on top of the pins. To remove the remaining gray areas, image binarization is applied to the contrast-adjusted image.

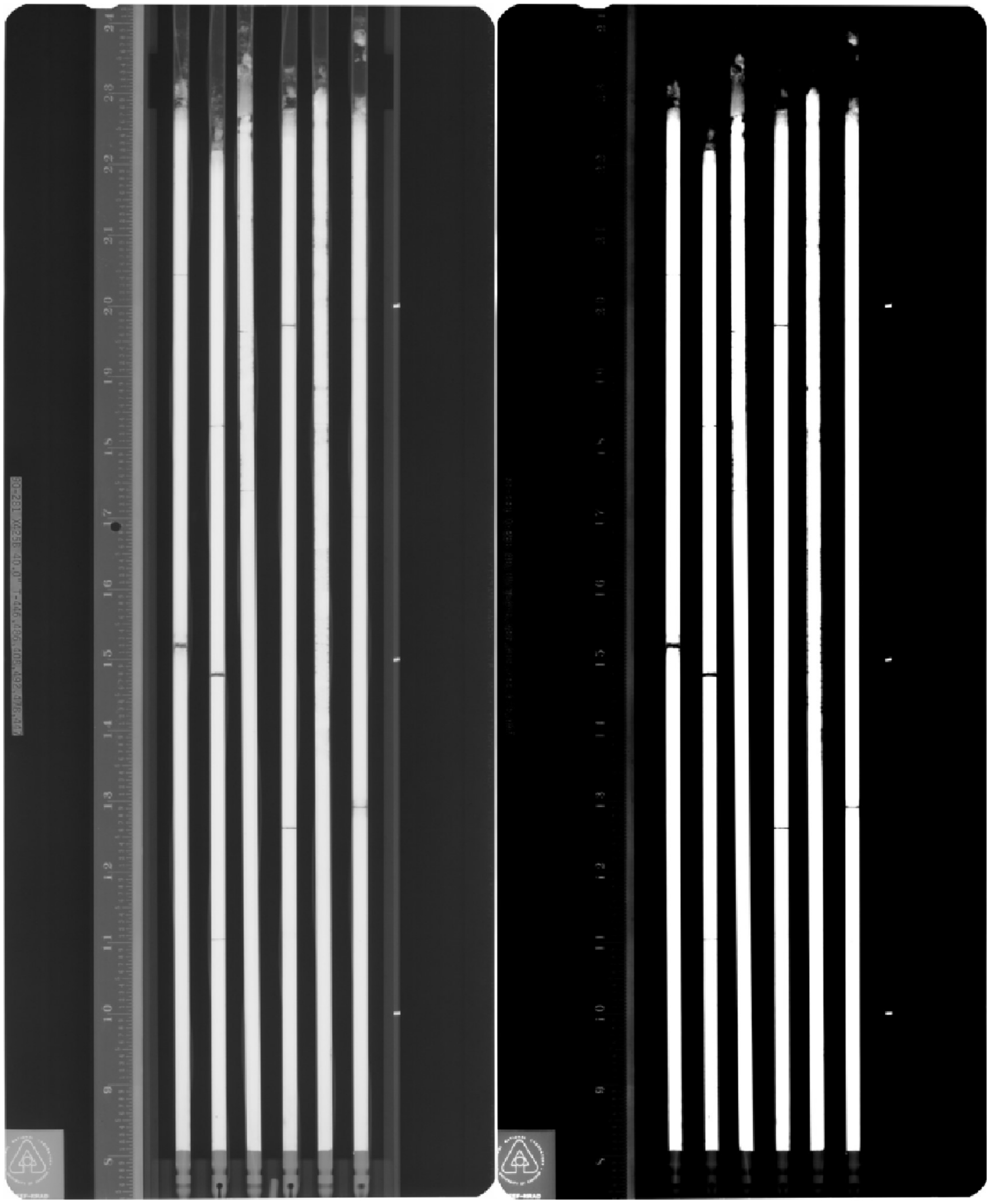

Fig.4 Original and contrast-adjusted radiography image of X425B pins T446, T486, T408, T492, T478, and T447. The original image is on the left and the contrast-adjusted image is on the right.

3.3 Image Binarization

While the pixel values for the contrast-adjusted image still range from 0 to 255, similar to the original image, binarization takes this process a step further and sets each pixel value to either 0 or 255, thereby converting it into a binary variable and making the whole image black and white. For this paper, threshold for the pixel value of 218 was selected using an image histogram analysis method similar to the one applied for contrast enhancement. Binarization can be considered as a primitive segmentation algorithm [23] when image objects are separated into two groups: background and foreground. Since the primary interest with the neutron radiographs is separating fuel pins from the background, binarization is ideally suited for this purpose, as it produces black and white image with pins segments in the foreground and the rest of the image in the background. This is shown in Figure 5.

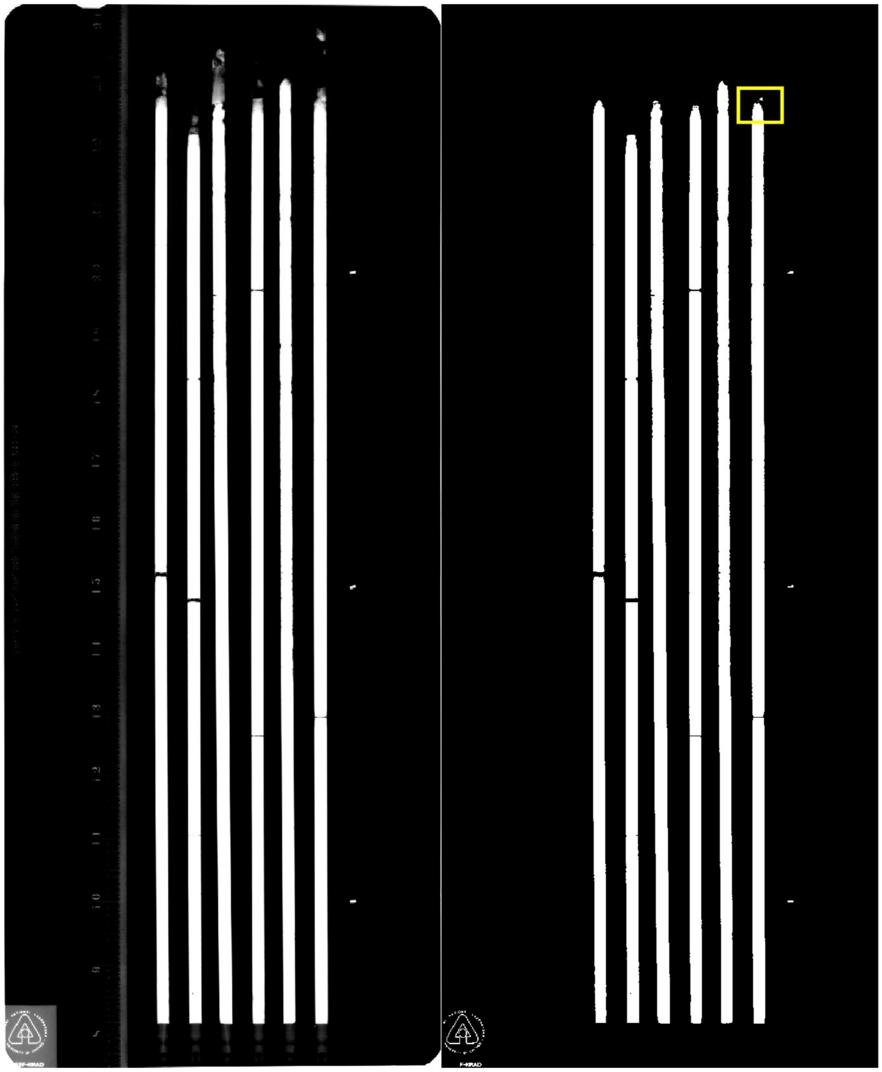

Figure 5. Side-by-side comparison of contrast-adjusted (left) and binary image (right) for radiography image of X425B pins T446, T486, T408, T492, T478, and T447. The yellow rectangle shows part of the image used to demonstrate the use of the connectivity and region-labeling algorithms.

As can be seen from Figure 5, the gray areas on the top of the fuel pins representing low-density and disintegrated fuel have been blacked out by setting the corresponding pixels to zero, while the solid areas of the fuel pins have been set to one. While image binarization is an effective tool for eliminating gray areas in the image, it cannot deal with small, isolated areas of high intensities, as shown in Figure 5. Since those areas have pixel values higher than the binarization threshold, they will survive the operation of binarization and their removal requires an additional step based on the size of the areas rather than pixel values. The pixels set to high in these images are called foreground or object pixels, while the pixels set to low are called background pixels. Finding connected areas of foreground and background pixels is subject of connectivity analysis. In Figure 5 the yellow rectangle shows the image area used to demonstrate connectivity analysis in the next section.

3.4 Image Connectivity Analysis

Image connectivity analysis is used in this paper to achieve two goals: (1) remove small, connected areas of high intensity pixels from the image; and (2) identify parts of the image representing the same fuel pin. As can be seen from Figure 5, some pins have cracks in them; however, the parts must be treated as a single object by the image processing algorithms. In image connectivity analysis, two major pixel neighborhood connectivity diagrams are used: 4-connectivity diagrams and 8-connectivity diagrams, as illustrated in Figure 6. The pixel of interest is marked as gray and it is counted as connected to its neighboring pixels if the pixel is a foreground pixel and touches its neighboring foreground pixels only along the edges for 4-connectivity analysis. For 8-connectivity analysis, it is counted as connected to its neighboring pixels if the pixel is a foreground pixel and touches its neighboring foreground pixels along the edges or on the corners. If any neighboring pixel is a background pixel, it is considered disconnected from the pixel of interest.

For this paper, 8-connectivity was used to find objects representing the continuous area in the image [24]. This selection was made to assure crisper edges for the foreground objects [23].

Figure 6. The 4-connectivity (left) and 8-connectivity (right) diagrams for neighboring pixels. The pixels marked black are considered connected to the pixel of interest marked gray.

An example of connectivity analysis is shown in Figure 7, which is the tip of fuel pin T447 from Figure 5. The area shown in Figure 7 is highlighted with a yellow rectangle in Figure 5. As can be seen from Figure 7, the top of the pin has several small high-intensity-connected components representing the "fluff." The connectivity algorithm segregated them as different objects—thus separating the main body of the fuel pin from its disintegrated parts. Having performed the connectivity analysis, the next step labels connected pixels—thus identifying separate objects in the image. Figure 7 in the right panel shows separate image regions that were labeled using a label equivalence resolving algorithm [25]. Each region or object is represented with a different color for better visualization. Label equivalence resolving algorithms are based on the idea of first scanning the image in a raster fashion using a mask. Each pixel is assigned a provisional label; however, after the first scan, some pixels of the same object may end up being assigned with two different labels. This is known as label collision. To eliminate label collision, all label collisions are stored in a table during the first scan. After the scan is completed, all label collisions are resolved using this table to correctly relabel the pixels based on connectivity analysis. During the labeling process, each region is assigned a numerical label, which is an integer number as illustrated in Figure 8. The value of each region labeling for the purpose of removing small areas of bright pixels is that after each labeled region, the total area of the region can be calculated and the regions with areas smaller than a preselected threshold can be set as the background. The result of area thresholding is shown in Figure 9, where the left panel shows the binary image produced by the binarization algorithm and the right panel is the binary image after applying the operation of area thresholding. The threshold was selected via analysis of the histogram of area sizes and set to 20K pixels (i.e., all regions with total area less than or equal to 20K pixels were set as the background). As can be seen, the small high intensity regions have been removed from the binary image, while the resulting image represents only the solid parts of the six fuel pins. The operation of area thresholding concludes the image segmentation and feature extraction part of the image processing pipeline.

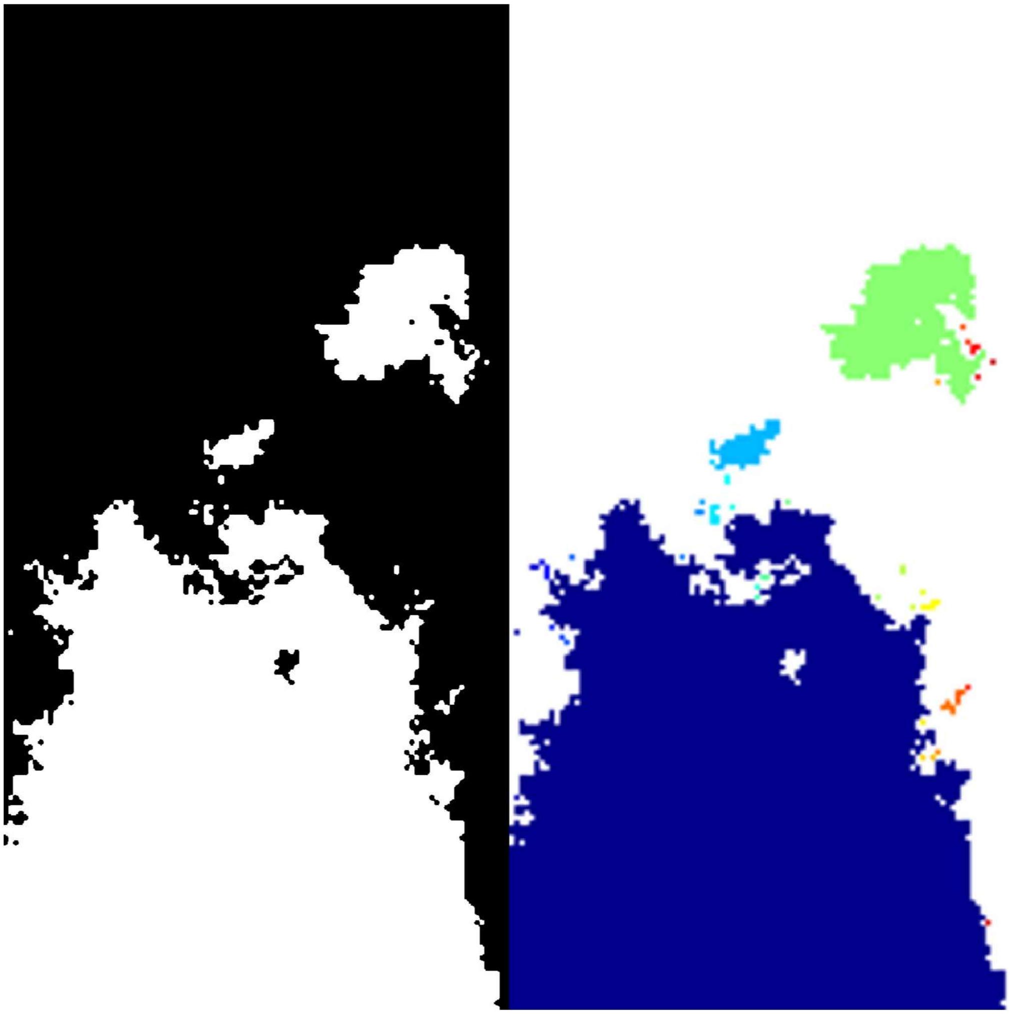

Figure 7. Connectivity of regions at the top of the fuel pin T447 (left panel) and connected components labeling (right panel) of those regions using a labeling algorithm. Each region is uniquely colored.

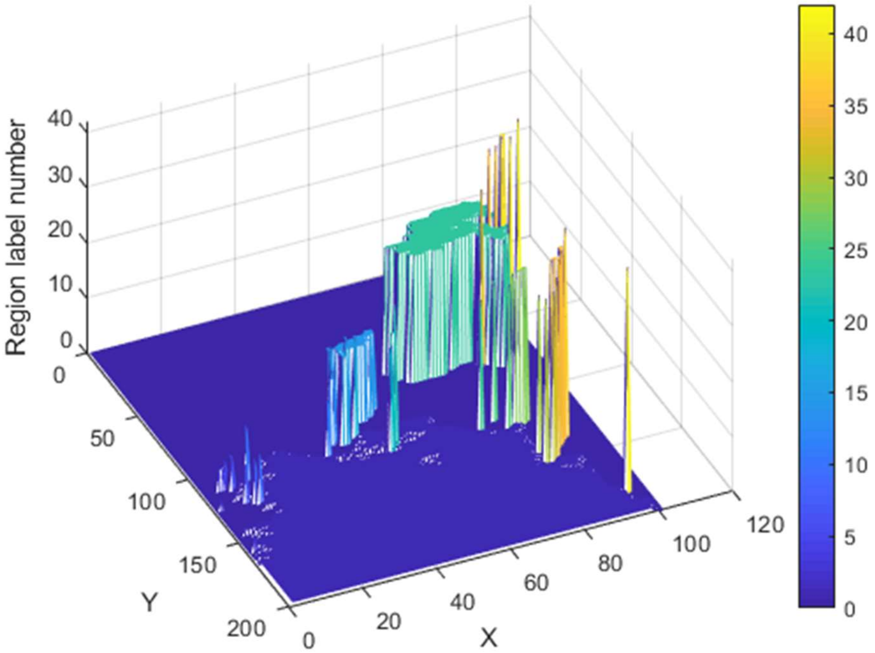

Figure 8. Three-dimensional representation of region labeling for the top of fuel pin T447.

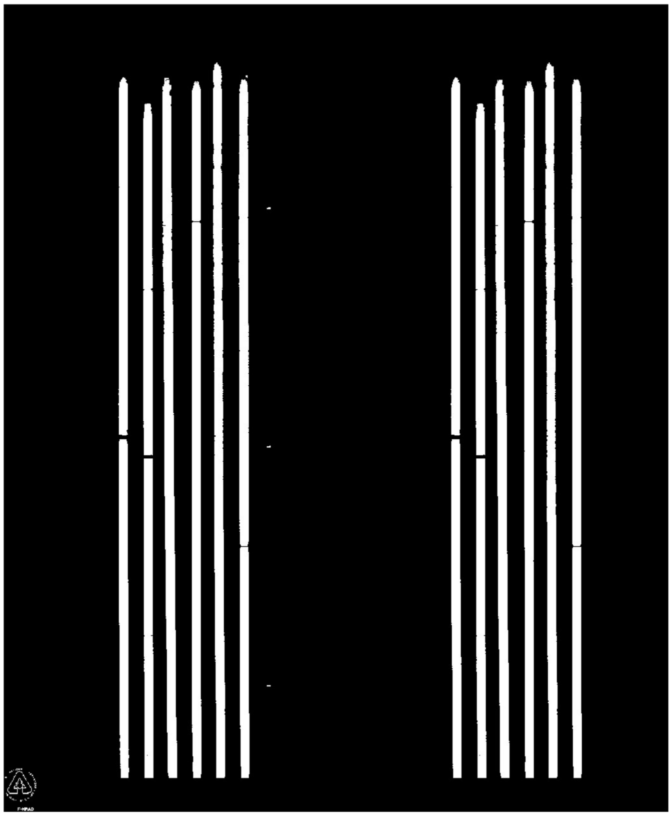

Figure 9. Side-by-side comparison of original binary image and the area thresholded binary image of X425B pins T446, T486, T408, T492, T478, and T447.

3.5 Identification of Fuel Pins

Having separated the fuel pins from the background, the next step is to identify individual pins and their parts on the area thresholded binary image. To achieve this, the same image connectivity analysis and region labeling has been applied to the area thresholded image. Since all small foreground objects were eliminated in the previous step, the connectivity analysis and labeling only labeled fuel pins and their parts, as shown in Figure 10.

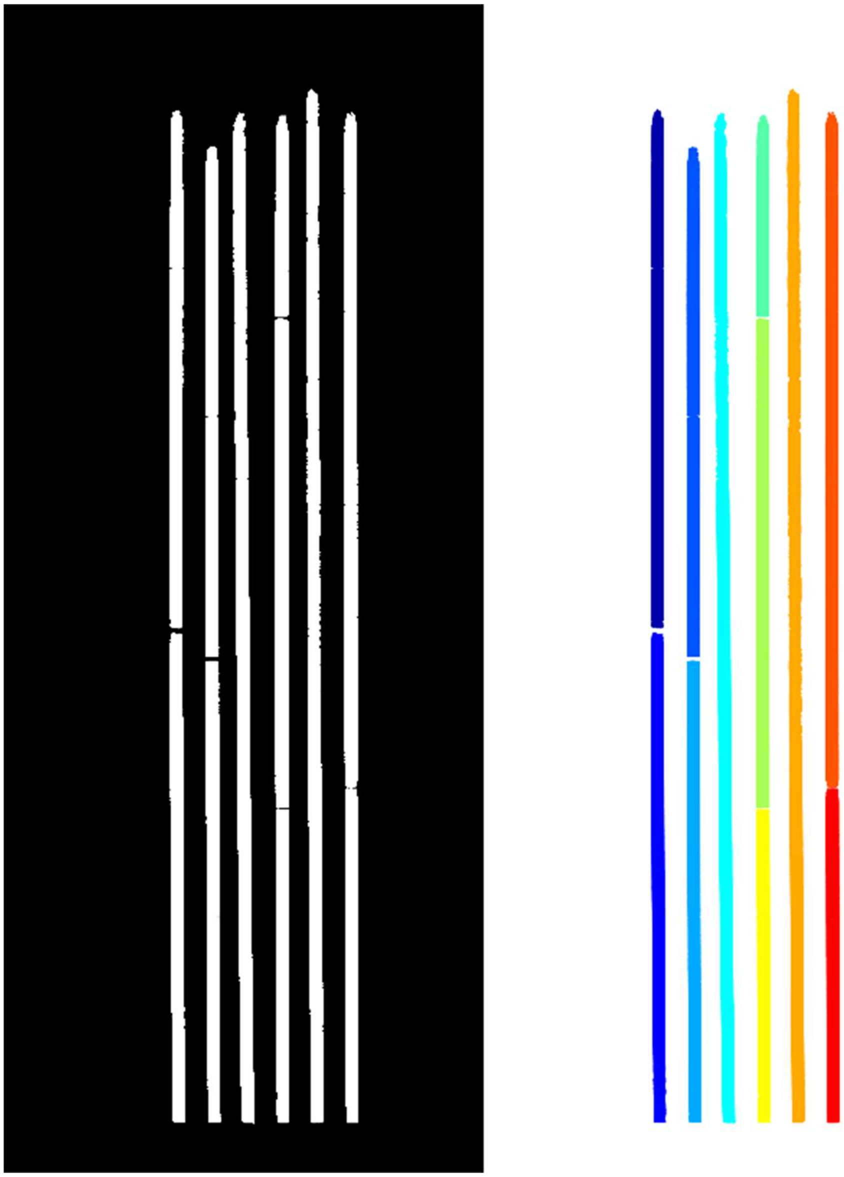

Figure 10. Area thresholded (left panel) and region labeled (right panel) of X425B pins T446, T486, T408, T492, T478, and T447.

Different image regions are color coded, and as is evident from Figure 10, the labeling algorithm discovered eleven separate regions due to cracks in some of the pins. Instead of 6 separate pins, the labeling algorithm discovered eleven regions, some of which need to be merged to be treated as a single pin. Also, to correctly calculate fuel axial growth, the cracks must be ignored as they do not contribute to actual fuel swelling. The first step is identifying the sizes of the different regions obtained after labeling algorithm.

This can be accomplished by finding bounding boxes for all regions, as shown in Figure 11. A bounding box is a rectangle that completely encompasses an image region and is used to describe region location on the image. It is based on extreme coordinates of an image region and those coordinates are byproducts of the region labeling algorithm.

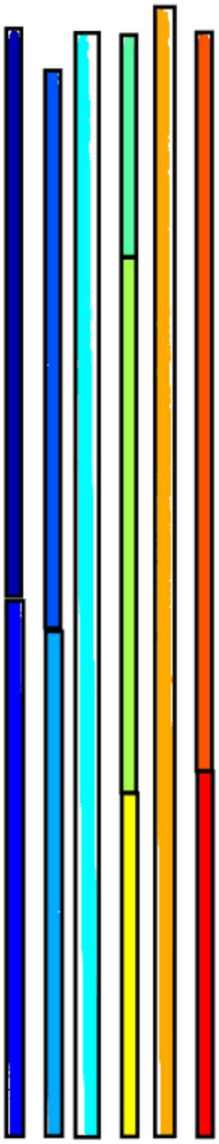

Figure 11. Region labeled image along with bounding boxes for different regions of X425B pins T446, T486, T408, T492, T478, and T447.

As can be seen in Figure 11, out of six fuel pins, only two—T408 and T478 —can be treated as single objects. All others have cracks splitting the fuel pins into two or even three parts. While calculations of pin length for one-piece pins is trivial, calculation of the length of the cracked pins is more involved and requires automatic identification of disjoint regions as a part of a single object. For the images on hand, this task is facilitated by the very nature of the objects as they are vertically placed rectangles parallel to each other without any complicated or overlaying intersecting shapes. This property of the original images allows for determining the center of mass of separate regions using a centroid finding algorithm. If each pixel is assigned a mass of unity, then the standard formula for a center of mass of a two-dimensional shape can be written as:

$$X_c = \frac{1}{N}\sum_{i=1}^{N} x_i, \quad Y_c = \frac{1}{N}\sum_{i=1}^{N} y_i \tag{2}$$

where X_c and Y_c are coordinates of the center of mass, N is the total number of pixels in the region, and x_i and y_i are coordinates of i^{th} pixel. Figure 12 shows the original image with bounding boxes and the locations of centroids marked with an asterisk. The different regions are enumerated from left to right.

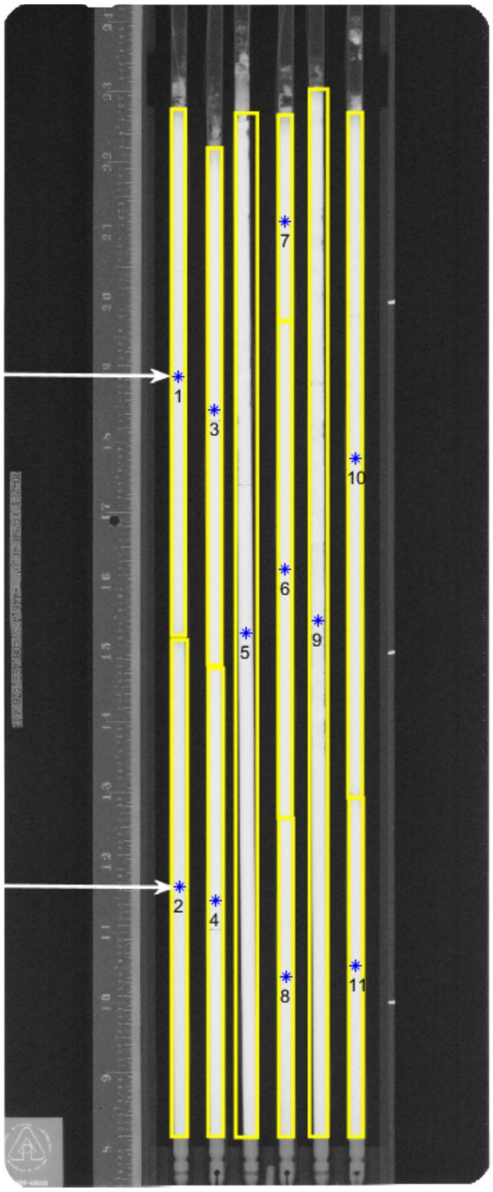

Figure 12. Original image of X425B pins T446, T486, T408, T492, T478, and T447, with superimposed bounding boxes, centroids locations, and region numbers. White arrows indicate the x-coordinates of the centroids for regions one and two.

To process the split pins as a single object, image regions were enumerated from left to right, as shown in Figure 12. Since the centroid coordinates were known, the image regions have been automatically grouped based on the x-coordinates of their centroids, as shown in Figure 12. Note that if regions belong to the same pin, their centroids have very similar x-coordinates. After grouping, the pins' lengths were calculated. Using corresponding bounding boxes, the lengths of the regions were added to obtain the total length of the fuel pin. For example, for Figure 12, the following lengths were obtained for the 11 different regions, as provided in Table 2.

Table 2. Length of different regions for image X425B, pins T446, T486, T408, T492, T478, and T447.

Region	1	2	3	4	5	6	7	8	9	10	11
Length [cm]	19.13	18.05	18.79	17.01	37.22	18.03	7.47	11.57	38.07	24.89	12.31

As can be seen from Table 2, two pins remained intact without any cracking during the experiment—T408 and T492—and their growth can be calculated in a straightforward manner using the bounding box dimensions. Prior to the length calculations, the size of the bounding boxes in pixels have been mapped to inches using the high precision ruler (e.g., 0.02 in. (0.051 cm) graduations) placed to the left of the pins in Figure 12. The others were grouped based on the x-coordinates of their centroids, and their length was determined as the sum of the lengths of the corresponding regions. Specifically, regions 1 and 2 were grouped as pin T446, regions 3 and 4 were grouped as pin T486, regions 6, 7, and 8 were grouped as pin T492, and regions 10 and 11 were grouped as pin T447. Table 3 provides a summary table of pin length characteristics for X425B.

Table 3. Initial and post-irradiation pin length for X425B, pins T446, T486, T408, T492, T478, and T447.

Pin ID	T446	T486	T408	T492	T478	T447
Fuel Composition	U-8Pu-10Zr	U-19Pu-10Zr	U-10Zr	U-8Pu-10Zr	U-10Zr	U-8Pu-10Zr
Initial Fuel Slug Length [cm]	34.44	34.37	34.34	34.31	34.31	34.37
Calculated Fuel Pin length [cm]	37.18	35.80	37.22	37.07	38.07	37.20

It is well known [4 – 7] that a negative correlation exists between axial fuel growth of U-Pu-Zr fuel and its Pu content (i.e., with higher Pu content a fuel slug will swell less). This is supported by the results presented in Table 3 as pin T486 with higher Pu content swells the least, while the U-10Zr pins exhibit the biggest growth with the U-8Pu-10Zr pin lying in between.

4. Results and Discussion

The image analysis algorithm described in previous sections was applied to 20 images, each containing six pins. Technical specifications for each pin are summarized in Table 1. Out of 120 pins, 77 are characterized as U-10Zr pins, 27 as U-8Pu-10Zr pins, and 16 as U-19Pu-10Zr pins. Figure 13 represents histograms of pins with different fuel compositions. The largest axial growth is observed for the binary fuel, while the smallest growth is observed for the U-19Pu-10Zr. This result is in agreement with previously reported studies [2 – 6]. For better evaluation of fuel growth, Figure 14 shows probability density functions (PDFs) for fuel growth, based on the same data shown in Figure 13. As can be seen, while the modes of the PDFs for U-10Zr and U-8Pu-10Zr are different, the two PDFs overlap significantly and have similar variances. The PDF for U-19Pu-10Zr is shifted significantly to the left and shows signs of being bimodal, which is not visible on the histogram in Figure 13.

The bimodal nature of U-19Pu-10Zr PDF is due to the large variance in U-19Pu-10Zr burnup values, which can be seen in Table 1. While the 77 U-10Zr pins and the 27 U-8Pu-10Zr pins have average burnup values at 10% with a variance of 0.15%, the U-19Pu-10Zr pins have an average burnup of 10% with a variance of 2.41%, which explains the bimodal nature of its PDF. The other compositions show no such bimodal distribution

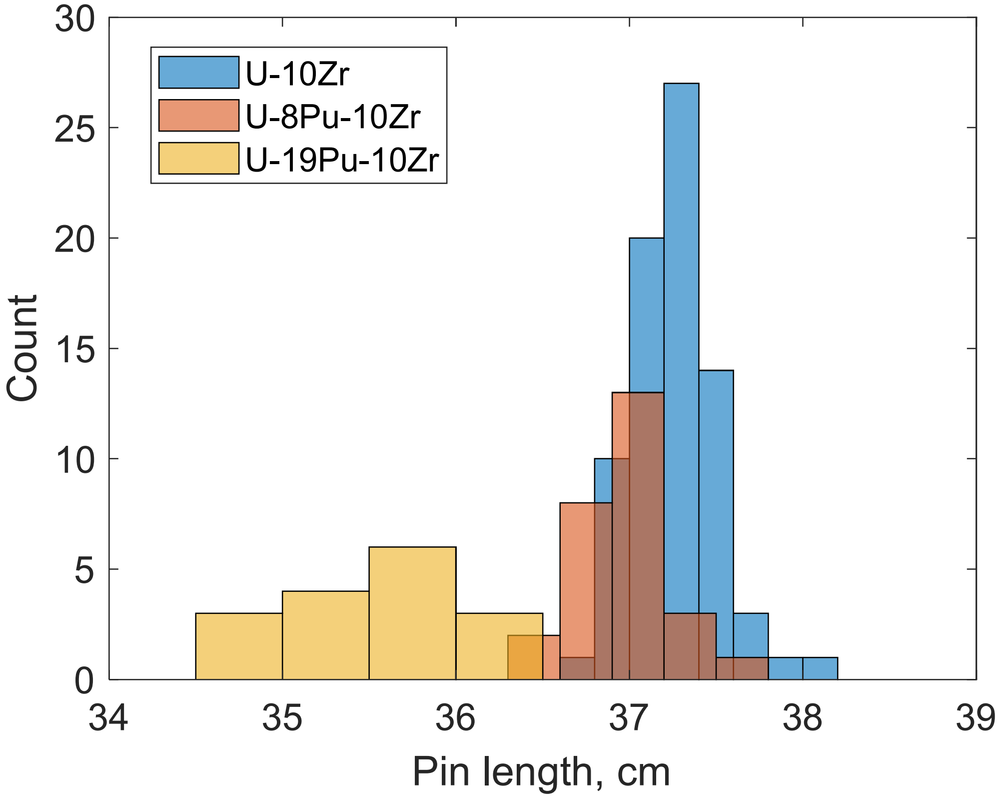

Figure 13. Histograms of the length of the 120 fuel pins.

While the PDFs for the U-10Zr and U-8Pu-10Zr pins have significant overlap, further statistical analysis reveals that the average growth for these two types of fuel is statistically different, as shown in Figures 14 and 15. Figure 14 shows the average pin length with 95% confidence intervals for three types of fuel, while Figure 15 shows the percentage of average fuel growth with 95% confidence intervals for the same types of fuel. For both parameters, the 95% confidence intervals do not overlap pointing to a statistically different swelling for U-10Zr and U-8Pu-10Zr. U-19Pu-10Zr pins demonstrate significantly lower swelling, as is evident from the figures.

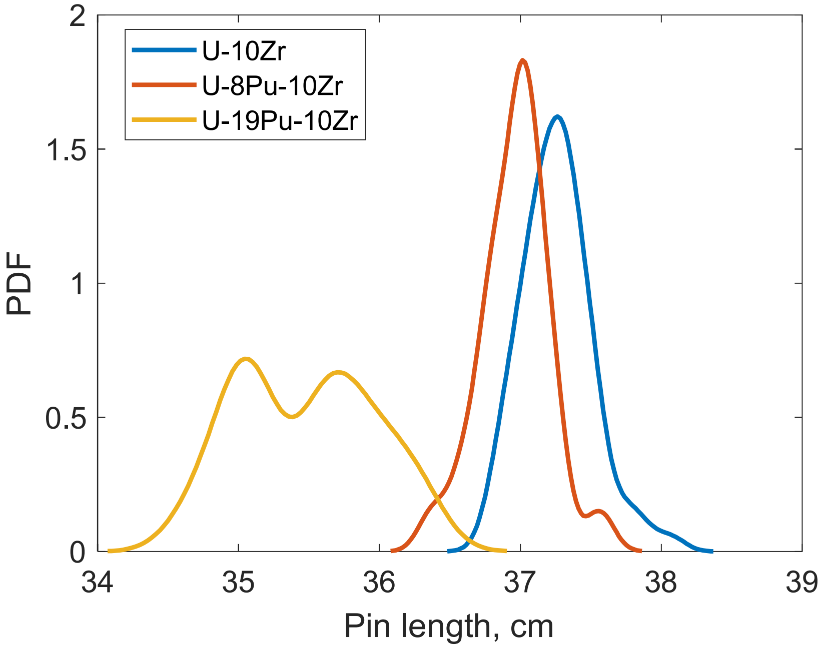

Figure 14. Probability density functions (PDF) for fuel slug length.

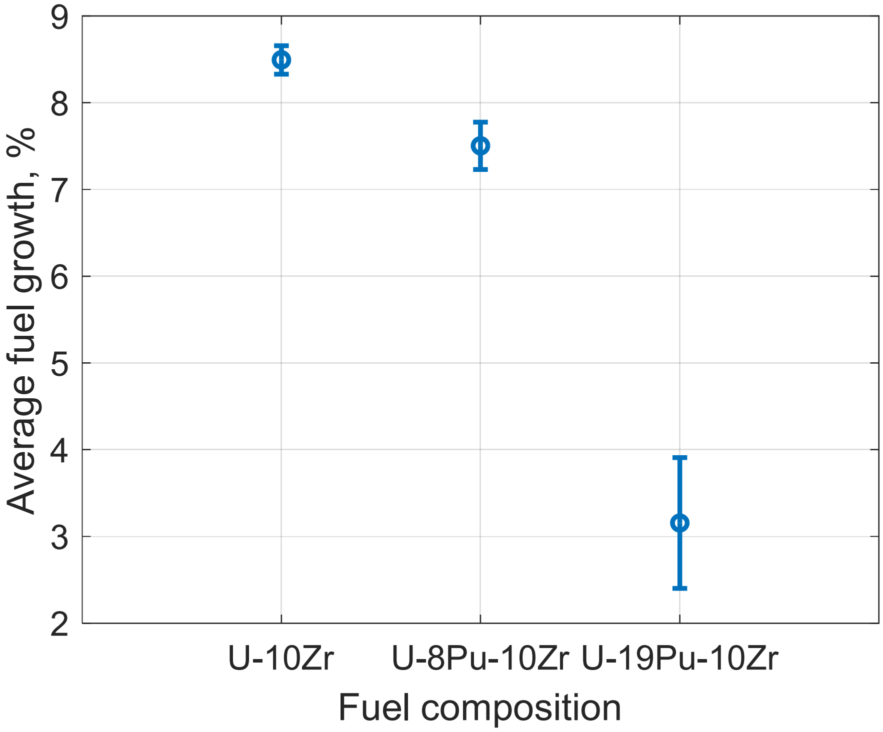

Figure 15. Average fuel slug length along with 95% confidence intervals for different fuel composition.

It has been shown using neutron radiographs of three types of fuel and 120 fuel pins that advanced image processing can be successfully applied to automatically evaluate the extent of axial fuel growth that is consistent with previously reported results obtained through visual examination. However, automatic image processing significantly reduces time for analysis and eliminates the human factor from determination of a fuel slug's axial growth. The algorithm opens the possibility to process thousands of neutron radiography images available in historical databases to accurately determine the dependence of fuel growth on fuel composition and burnup. These empirical dependencies can be used to improve and refine existing fuel performance codes to develop assessment cases for next generation reactors.

The average growth for U-10Zr was 8.66% 95 %CI [8.50 – 8.82], for U-8Pu-10Zr it was 7.80% 95%CI [7.5260 – 8.0792], and for U-19Pu-10Zr it was 3.46% 95%CI [2.6912 – 4.2203], which is consistent with Ref. [8].

5. Conclusions

A fully automated image analysis algorithm has been developed and validated to determine the degree of axial fuel growth based on neutron radiographs. The proposed algorithm has been applied to 120 pins of three different fuel compositions: U-10Zr, U-8Pu-10Zr, and U-19Pu-10Zr. The algorithm robustly identified the axial swelling for the fuel slugs—even for cracked slugs. The degree of axial swelling was found to be consistent with previously reported results obtained by visual examination. In contrast to all previous work on neutron radiograph image analysis, the algorithm can quickly analyze thousands of images producing results of fuel axial swelling. The fuel axial swelling measurements obtained from this study will be used in conjunction with the BISON fuel performance code to support and advance fuel qualification and future model development.

References

1. D. C. Crawford, D. L. Porter, and S. L. Hayes, “Fuels for sodium-cooled fast reactors: U.S. perspective,” Journal of Nuclear Materials 371 (2007) 202–231.
2. D. C. Crawford, D. L. Porter, S. L. Hayes, M. K. Meyer, D. A. Petti, and K. Pasamehmetoglu, “An approach to fuel development and qualification,” Journal of Nuclear Materials 371 (2007) 232–242.
3. Idaho National Laboratory, “Nuclear Materials Experiments Execution Process,” LWP-20700, Rev. 1, Lab-wide Procedure, Manual: 20 – Research Management System, June 2017.
4. D. L. Porter and H. Tsai, “Full-length U-xPu-10Zr (x=0, 8, 19) fast reactor fuel pin test in FFTF,” Journal of Nuclear Materials, 427 (2012) 46–57.
5. D. L. Porter, H. J. M. Chichester, P. G. Medvedev, S. L. Hayes, and M. C. Teague, “Performance of low smeared density sodium-cooled fast reactor metal fuel,” Journal of Nuclear Materials 465 (2015) 464–470.
6. H. Tsai, A. B. Cohen, M. C. Billone, and L. A. Neimark, “Irradiation performance of U-Pu-Zr metal fuels for liquid-metal-cooled reactors,” Proceedings of the 3rd International Conference on Nuclear Engineering (ICONE-3), Kyoto, Japan, 23–27 April 1995.
7. R. G. Pahl, C. E. Lahm, and S. L. Hayes, “Performance of HT9 clad metallic fuel at high temperature,” Journal of Nuclear Materials 204 (1993) 141–147.
8. G. L. Hofman, R. G. Pahl, C. E. Lahm, and D. L. Porter, “Swelling behavior of U-Pu-Zr fuel,” Metallurgical Transactions 21A (1990) 517–520.
9. G. L. Hofman, L. C. Walters, and T. H. Bauer, “Metallic fast reactor fuels,” Progress in Nuclear Energy 31 (1997) 83–110.

10. J. Galloway, C. Unal, N. Carlson, D. Porter, and S. Hayes, “Modeling constituent redistribution in U-Pu-Zr metallic fuel using the advanced fuel performance code BISON,” Nuclear Engineering and Design 286 (2015) 1–17.
11. M. R. Tonks, D. Schwen, Y. Zhang, P. Chakraborty, X. Bai, B. Fromm, J. Yu, M. C. Teague, D. A. Andersson, “Assessment of MARMOT: A Mesoscale Fuel Performance Code,” INL/EXT-15-35108, April 2015, p. 38–41.
12. A. E. Craft, B. A. Hilton, and G. C. Papaioannoua, “Characterization of a neutron beam following reconfiguration of the neutron radiography reactor (NRAD) core and addition of new fuel elements,” Nuclear Engineering and Technology 48(1) (2016) 200–210.
13. S. Renukalatha and K. V. Suresh, “A review on biomedical image analysis,” Biomedical Engineering: Applications, Basis, and Communications 30(4) (2018) 1830001.
14. L. Duval, M. Moreaud, C. Couprie, D. Jeulin, H. Talbot, and J. Angulo, “Image processing for materials characterization: Issues, challenges and opportunities,” 2014 IEEE International Conference on Image Processing (ICIP), Paris, France, 27–30 October 2014.
15. D. Sitaram, N. Padmanabha, S. S. Shibani, “Still image processing techniques for intelligent traffic monitoring,” 2015 Third International Conference on Image Information Processing (ICIIP), Waknaghat, India, 21–24 December 2015.
16. BT.601: Studio encoding parameters of digital television for standard 4:3 and wide screen 16:9 aspect ratios". ITU.
17. W. Gong, P. Trtik, A. W. Colldeweih, L. I. Duarte, M. Grosse, E. Lehmann, and J. Bertsch, “Hydrogen diffusion and precipitation in duplex zirconium nuclear fuel cladding quantified by high-resolution neutron imaging,” Journal of Nuclear Materials 526 (2019) 151757.
18. C. Ly, C. Vachet, I. Schwerdt, E. Abbott, A. Brenkmann, L. W. McDonald, and T. Tasdizen, “Determining uranium ore concentrates and their calcination products via image classification of multiple magnifications,” Journal of Nuclear Materials 533 (2020) 152082.
19. J.-L. Lin, W. Zhong, H. Z. Bilheux, and B. J. Heuser, “Azimuthally anisotropic hydride lens structures in Zircaloy 4 nuclear fuel cladding: High-resolution neutron radiography imaging and BISON finite element analysis,” Journal of Nuclear Materials 496 (2017) 129–139.
20. R. Collette, J. King, C. Buesch, D. D. Keiser Jr., W. Williams, B. D. Miller, and J. Schulthess, “Analysis of irradiated U-7wt% Mo dispersion fuel microstructures using automated image processing,” Journal of Nuclear Materials 475 (2016) 94–104.
21. G. W. Helmreich, D. R. Brown, T. J. Gerczak, and J. D. Hunn, “Quantification of silicon carbide grain structure in TRISO fuel by BSE image analysis,” Journal of Nuclear Materials 533 (2020) 152075.
22. J. M. Harp, D. L. Porter, B. D. Miller, T. L. Trowbridge, and W. J. Carmack, “Scanning electron microscopy of a fast flux test facility irradiated U-10Zr fuels cross section clad with HT-9,” Journal of Nuclear Materials 494 (2017) 227–239.
23. R. C. Gonzalez and R. E. Woods, Digital Image Processing, Addison-Wesley, Reading, Massachusetts, 1993.
24. L. He, X. Ren, Q. Gao, X. Zhao, B. Yao, and Y. Chao, “The connected-component labeling problem: A review of state-of-the-art algorithms,” Pattern Recognition 70 (2017) 25–43.
25. L. He, Y. Chao, and K. Suzuki, “Two efficient label-equivalence-based connected–component labeling algorithms for three-dimensional binary images,” IEEE Trans. Image Process. 20(8) (2008) 2122–2134.